Chapter 3

Studies on some spinel oxides based electrocatalysts for oxygen evolution application

3.1 Introduction

Electrocatalysis of water to produce molecular oxygen and hydrogen is the most promising way to produce clean and renewable energy. Water splitting is combination of mainly two half reactions, hydrogen evolution and oxygen evolution reaction (OER). The OER is the key half-cell reaction in the water splitting process essential for electrochemical energy conversion and storage systems such as water electrolyzers and hydrogen fuel cells [121-124]. OER is basically four electrons and four protons coupled electrochemical reaction and requires very high overpotential. The most promising route for renewable hydrogen production is the direct electrolysis of water to form molecular hydrogen and oxygen. Unfortunately, the sluggish kinetics of the oxygen evolution reaction (OER, $4OH^- \rightarrow 2H_2O + O_2 + 4e^-$ in base and $2H_2O \rightarrow 4H^+ + O_2 + 4e^-$ in acid) entails large reaction overpotentials, fundamentally restraining the overall efficiency of this process. In an alkaline medium, OER is very sluggish and requires a very large overpotential [125, 126]. For OER, noble metal oxides such as RuO_2 and IrO_2, Rh-Pt have been extensively used due to their better catalytic performance, as they are reported as the best catalysts for OER [127-133]. Since these catalysts are too costly to commercialize at a large scale, therefore, there is a need to develop cheaper and more versatile catalyst to replace these precious catalysts in large-scale industrial applications. The hunt for non-precious electrocatalysts for drastically reducing the overpotential and accelerating multistep proton-coupled electron transfer in OER has become a main aim for producing clean energy. While developing catalysts for OER, not only catalysts price but its abundance and overpotential for OER must be considered. Due to their controllable composition, morphology, structure and abundance of raw materials, great attention has

been paid for the development of spinel-based catalysts for water splitting and energy storage applications [134, 61, 135]. Numerous OER electrocatalysts, such as Co_3O_4, nickel oxides/oxyhydroxides, mixed metal hydroxides/oxides, layered double hydroxide (LDH) based, spinel ferrites, denoted as MFe_2O_4 (M = Co, Ni, Mn, Cu, Zn, etc.), [136, 137, 58, 138-140] are a kind of binary/ternary metal oxide, are very fascinating as they are cost-effective and earth-profuse, and possess many noteworthy properties, such as magnetism, catalysis etc.

To date, numerous methodologies have been adopted for the synthesis of spinel-based catalysts such as solvothermal, hydrothermal, thermal decomposition and solid-state synthesis etc. but most of the methods are complicated and time-consuming. Herein, we have adopted the sol-gel technique for the synthesis of the catalysis. In comparison to other methods, sol-gel is relatively simple and requires less time for catalyst preparation. In the present work, we have prepared $NiFe_2O_4$ (NFO), $CoFe_2O_4$ (CFO), and $CoNiFe_2O_4$ (CNFO) by facile sol-gel method and used the same for OER application in an alkaline medium. The first time we prepared CNFO by sol-gel technique and catalytic performance of CNFO was found to be superior or comparable to NFO and CFO. The superior performance of the CNFO could be due to increased oxygen vacancy which was observed through XPS and BET measurement.

3.2 Results and discussion

3.2.1. Analysis by FTIR

The FTIR spectra of NFOs (NFO-600, NFO-700, NFO-800 and NFO-800) and cobalt-doped nickel ferrite CNFO-800 have been shown in Figure 3.1 in which the stretching vibrations observed around 670 cm^{-1} and 576 cm^{-1} corresponds to Fe-O bond vibration in octahedral and Ni-O bond in tetrahedral sites, respectively [141, 142]. Vibrations observed around 1633 cm^{-1} and 1036 cm^{-1} correspond to carboxylate and traces of

nitrates. Doublet peaks observed around 2341 cm^{-1} and 2361 cm^{-1} are due to the resonances of traces of absorbed atmospheric CO_2, whereas the broad peak observed around 3455 cm^{-1} agrees with O-H stretching vibrations of intercalated water molecules [143].

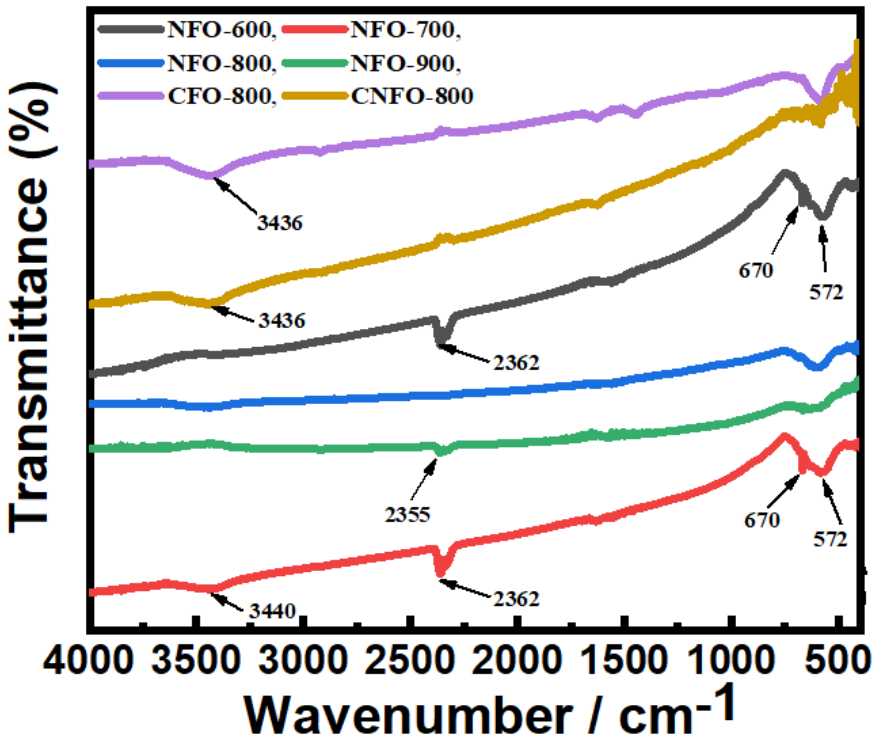

Figure 3.1 FTIR spectra of NFO-600, NFO-700, NFO-800, NFO-900, CFO-800 and CNFO-800.

3.2.2 Structural analysis using X-ray diffraction

Structural studies of the prepared samples of $Co_xNi_{1-x}Fe_2O_4$ spinel ferrites were performed by X-ray diffraction technique. The room temperature X-ray diffraction (XRD) patterns for $Co_xNi_{1-x}Fe_2O_4$ spinels (with x = 0, 0.5 and 1) are shown in [Figure 3.2 (a)]. The samples of $Co_xNi_{1-x}Fe_2O_4$ ferrites with x = 0, 0.5 and 1 are denoted by NFO, CNFO, and CFO, respectively. The XRD patterns present the formation of the spinel phase of ferrite with a cubic structure having $Fd\bar{3}m$ space group. However, all the XRD patterns have some additional phases. The XRD pattern of CFO contains phases of $CoFe_2O_4$ (PCPDF No. 03-0864) and Co_3O_4 (PCPDF No. 42-1467 and denoted by *),

CNFO contains phases of (Co, Ni)Fe_2O_4, Co_3O_4 and $Fe_{0.872}O$ (PCPDF No. 71-0161 and denoted by #) and NFO contains phases of $NiFe_2O_4$ (PCPDF No. 46-2267) and $Fe_{0.872}O$. Similar results were also observed by earlier authors [144]. Further, in the XRD patterns, the intensity of the most intense Bragg's peak is less compared to the other Bragg's peaks which may be due to texturing of the samples [145]. All Bragg's peaks of various phases were fitted using Le-Bail fit method using FullProf Suite [146]. [Figure 3.2 (b)-(d)] represent Le-Bail fits of XRD patterns for $Co_xNi_{1-x}Fe_2O_4$ spinel ferrites for x = 0, 0.5 and 1, respectively, in which solid dots (red color) were used to present observed XRD pattern while the calculated pattern was shown by continuous line (black color) just over observed pattern and lower continuous line (magenta color) shows difference between observed and calculated patterns. The vertical bars (blue color) demonstrate the position of Bragg's peaks in the XRD patterns of the prepared samples. In [Figure 3.2(b)] upper and lower vertical bars represent Bragg' peak position for $CoFe_2O_4$ and Co_3O_4 phases, respectively. In [Figure 3.2(c)] upper, middle and lower vertical bars stand for Bragg' peak position for (Co, Ni)Fe_2O_4, Co_3O_4, and $Fe_{0.872}O$ phases, respectively. In [Figure 3.2(d)] upper and lower vertical bars represent Bragg's peak position for $NiFe_2O_4$ and $Fe_{0.872}O$ phases, respectively. The lattice constant "a" and unit cell volume "V" for CFO and NFO for $Fd\bar{3}m$ space group were found to be equal to a = 8.3965(6) Å, V = 591.96(7) $Å^3$ and a = 8.342(1) Å, V = 580.6(1) $Å^3$, respectively, which decrease due to the difference in the ionic size of Co^{2+} (r = 0.58 Å) and Ni^{2+} (r = 0.55 Å) ions [147].

3.2.3 X-ray photon spectroscopic studies

To get further intuition into the surface composition of the samples we have performed XPS analysis of NFO-800, CFO-800 and CNFO-800. Survey spectra of all the sample which shows the elemental composition have been shown in Figure 3.3. Figure 3.4 shows the Ni 2p [Figure 3.4(a)], Fe 2p [Figure 3.4(b)], O1s [Figure 3.4(c)] and C1s [Figure

3.4(d)] core level spectra NFO-800. It was found that Ni $2p_{3/2}$ signal appeared at 856.0 eV, with a satellite peak at 862.18 eV, and the peak observed at 873.74 eV was ascribed to the Ni $2p_{1/2}$ level [148]. The Auger electron peaks of Ni at observed 879.44 eV elucidates presence of Ni ion in +2 oxidation state [Figure 3.4(a)].

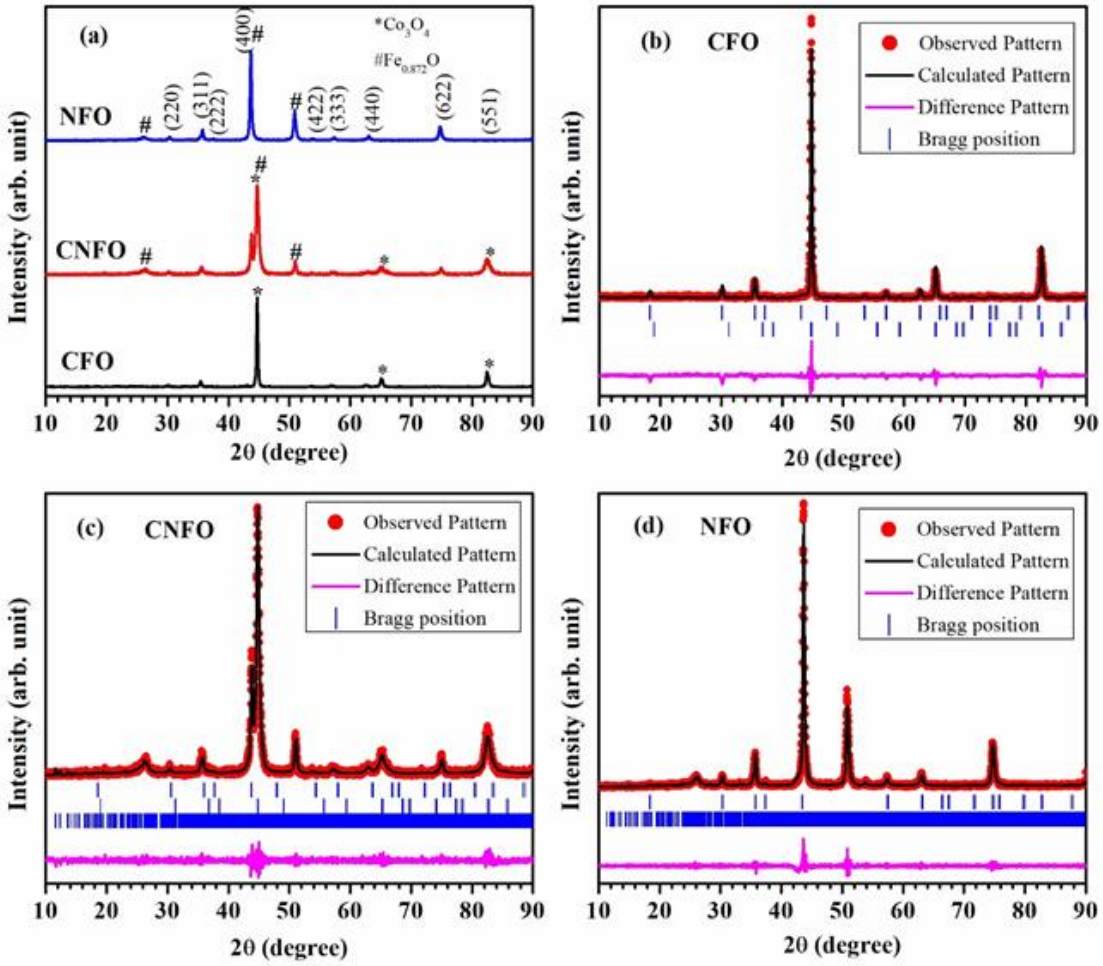

Figure 3.2 (a) Room temperature powder X-ray diffraction patterns for $Co_xNi_{1-x}Fe_2O_4$ spinel ferrites (with x = 0, 0.5 and 1) calcined at 800 °C for 3 hours in N_2 atmosphere. The Le-Bail fits for (b) CFO, (c) CNFO and (d) NFO spinel ferrites.

For Fe $2p_{3/2}$ [Figure 3.4(b)], two peaks were observed at 710.85 and 712.63 eV, suggesting the occupation of octahedral and tetrahedral sites respectively and the one satellite peak observed at 718.89 eV confirms the existence of Fe^{3+}. For O1s, [Figure 3.4(c)] two peaks were observed at 530.41 and 532.13, which signs the existence of Ni(II)−O and Fe(III)−O chemical bonds in NFO-800, constituent band with a peak

position at 532.13 eV indicate the presence of the metal hydroxides [e.g., $Ni(OH)_2$, $Fe(OH)_3$]. A broad C1s [Figure 3.4(d)] shows three different peaks at 284.64, 286.75 and 289.96 eV which correspond to C=C (C-C), C-O and O-C=O groups respectively.

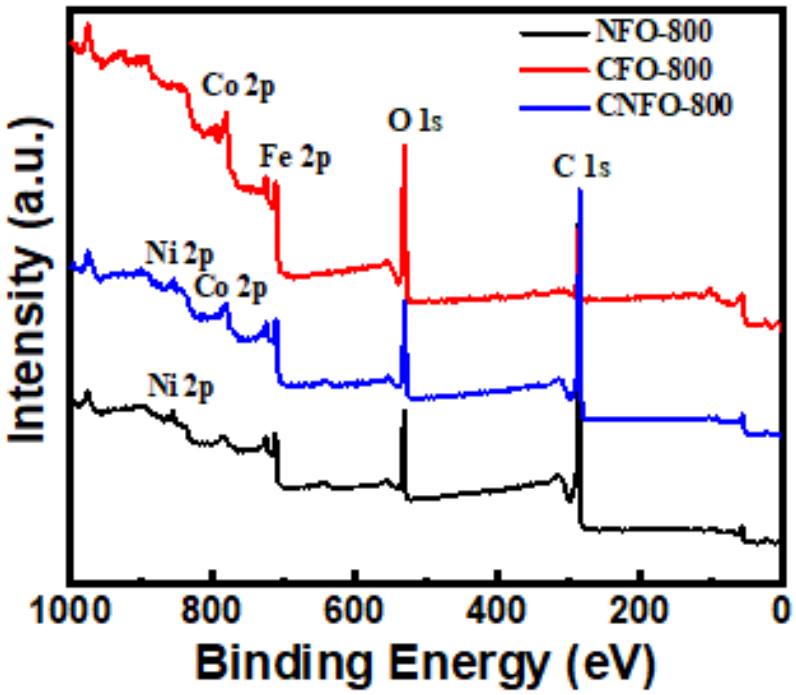

Figure 3.3 Combined XPS survey spectra of NFO-800, CFO-800 and CNFO-800.

XPS survey of CFO-800 and deconvoluted high-resolution spectra of Co 2p, Fe 2p, O 1s and C 1s are shown in Figure 3.3 and Figure 3.5. In the case of Co 2p [Figure 3.5(a)] spectra, the signals observed at 780.45 and 796.34 eV correspond to Co $2p_{3/2}$ and Co $2p_{1/2}$ which indicates the presence of Co^{2+} ions. The $Co2p_{3/2}$ peaks at 780.45 and 782.54 eV indicate the presence of Co^{2+} ions in octahedral and tetrahedral sites, respectively. One satellite peak observed at 786.86 eV corresponds to Co $2p_{3/2}$, and it is consistent with the previous report [148, 149]. Here, in this case, Fe 2p spectrum [Figure 3.5(b)] is same as in NFO-800. The O 1s core-level [Figure 3.5(c)] and C1s [Figure 3.5(d)] XPS spectra for CFO-800 also displayed similar features as NFO-800.

Similarly the deconvoluted high resolution spectra of Ni 2p, Co 2p, Fe 2p, C 1s and O1s

in CNFO-800 is shown in Figure 3.6. Here, in this case, Co $2p_{3/2}$ peak [Figure 3.6(a)] is broader than in the CFO-800. This difference could probably be due to the higher nuclear effective charge of the d electrons of the Ni^{2+} than for the Co^{2+} cations. It is evident from Figure 3.4(c), Figure 3.5(c) and Figure 3.6(e), the BE of the 1s orbital of the oxygen atoms in NFO-800, CFO-800 and CNFO-800 is 530.41 eV, 529.80 eV and 530.16 eV respectively. The difference in the binding energy of O1s orbital is fully related to the basicity of inorganic compounds [148-150]. Electron donation ability by the oxide becomes higher as the binding energy of O 1s decreases, and this electron-donation capability must be considered to judge the chemical reactivity of the oxide surface [149, 150]. The binding energy of O 1s orbital in NFO-800 and CNFO-800 is very close, so no significant difference in their catalytic performance was observed.

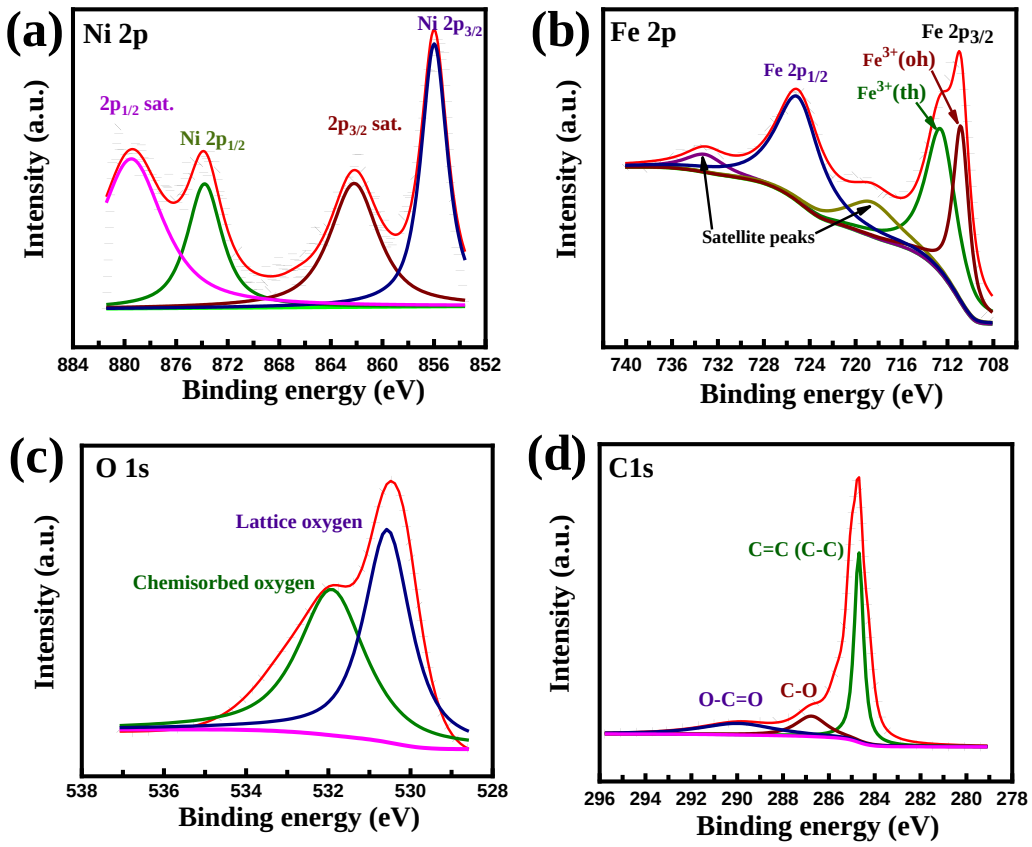

Figure 3.4 XPS profile of (a) Ni 2P, (b) Fe 2p, (c) O 1s, and (d) C 1s in NFO-800.

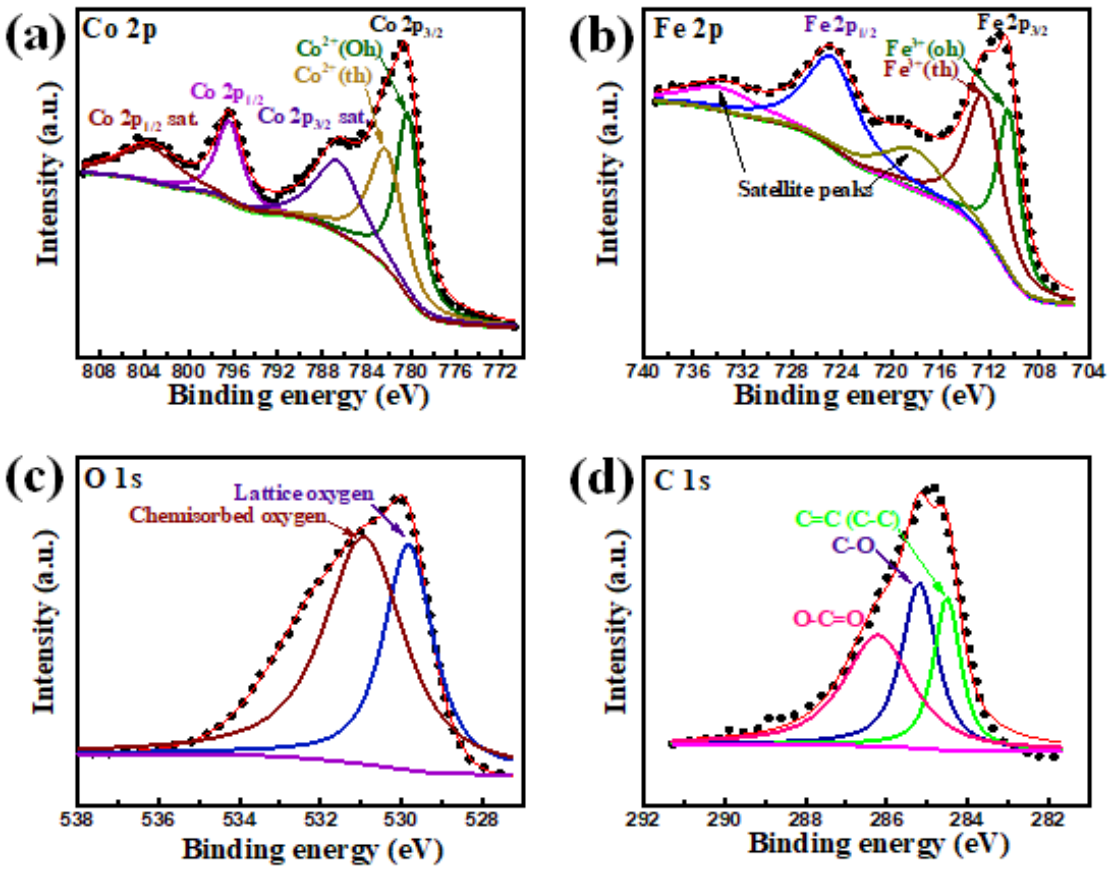

Figure 3.5 XPS profile of (a) Co 2P, (b) Fe 2p, (c) O 1s, and (d) C 1s in CFO-800.

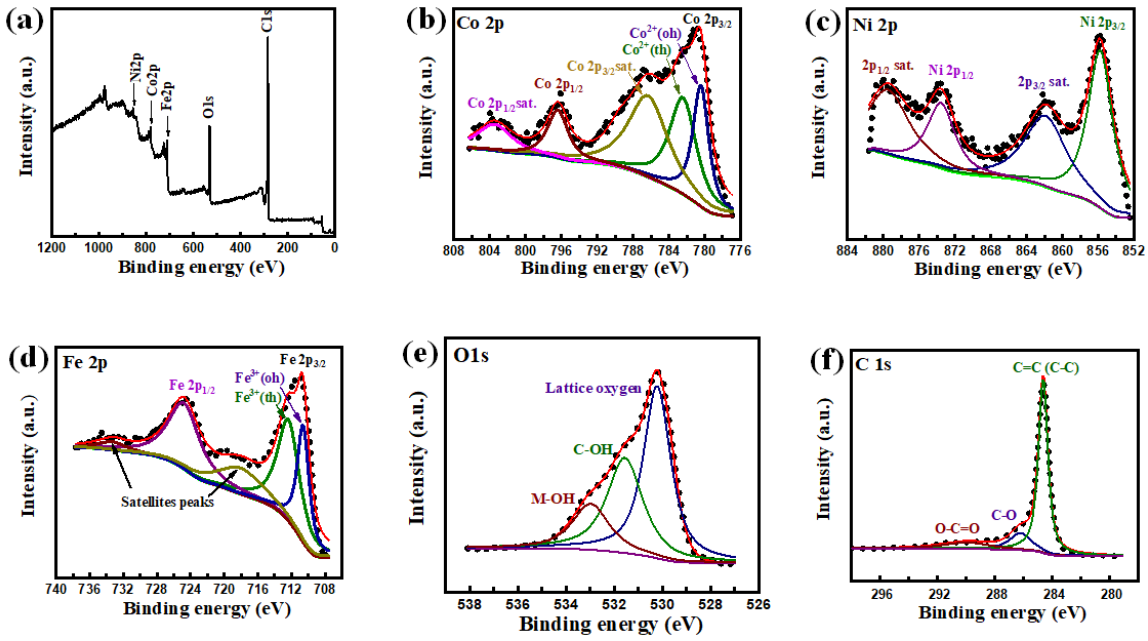

Figure 3.6 XPS profile of (a) Co 2P, (b) Ni 2p, (c) Fe 2p, (d) O 1s, and (e) C 1s in CNFO-800.

3.2.4 BET and SEM Study

To get better information about the porous nature of as-prepared catalysts, surface area, pore size, pore volume and pore size distribution were assessed through the BET and BJH methods. Figure 3.7 shows the N_2 adsorption-desorption isotherm and respective pore size distribution from BJH plots for CFO-800, NFO-800 and CNFO-800. Isotherm plots resemble Type IV and are in good agreement with previous reports. A detail of BET measurements is given in Table 3.1. The BET surface area of the prepared materials is very similar to Han et al. in which they have utilized iron-based spinel for OER application [151]. NFO-800 and CNFO-800 have almost similar average pore diameter and surface area which were found to be comparatively smaller as compared to CFO-800. SEM images of NFOs prepared at various temperatures have been shown in Figure 3.8. From the figures, it is very clear that as the temperature increases from 600 to 800 °C [Figure 3.8 (a-c)], the morphology changes from granular to aggregated type and beyond this temperature (at 900 °C) structural morphology gets collapse [Figure 3.8(d)]. Further Figures 3.8(e) and 3.8(f) show the SEM images of cobalt-doped NFO (CFO-800 and CNFO-800,) respectively. As we can see, in the case of CFO-800 [Figure 38(e)] very large particles were formed, and the surface morphology of CNFO-800 [Figure 3.8(f)] was found to be very similar to NFO-800 [Figure 3.8(c)]. Surface morphology and composition play a very important role in OER performance. EDAX and elemental mapping of all as-prepared catalysts have been given in Figures 3.9 to 3.14.

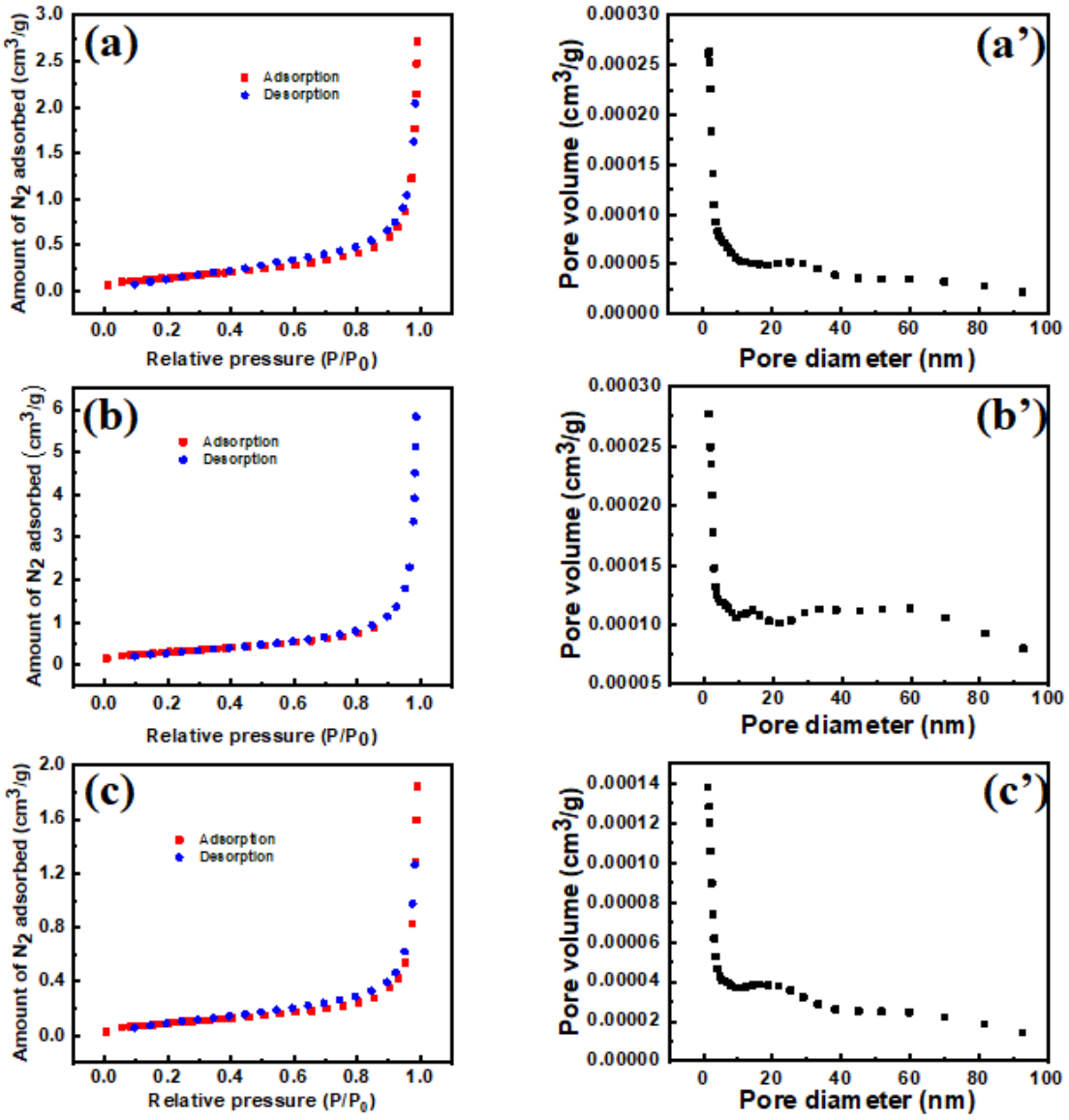

Figure 3.7 N_2 adsorption-desorption isotherms of (a) NFO-800, (b) CFO-800, (c) CNFO-800, and the corresponding NL-DFT pore size distribution (a') NFO-800, (b') CFO-800, and (c') CNFO-800.

Table 3.1 BET surface area and other parameters of NFO-800, CNFO-800 and CFO-800.

Sample	BET surface area ($m^2 g^{-1}$)	Pore Volume ($cm^3 g^{-1}$)	Pore diameter (nm)
NFO-800	0.5467	0.003931	28.7
CNFO-800	0.365	0.002659	29.1
CFO-800	1.10	0.01	36.71

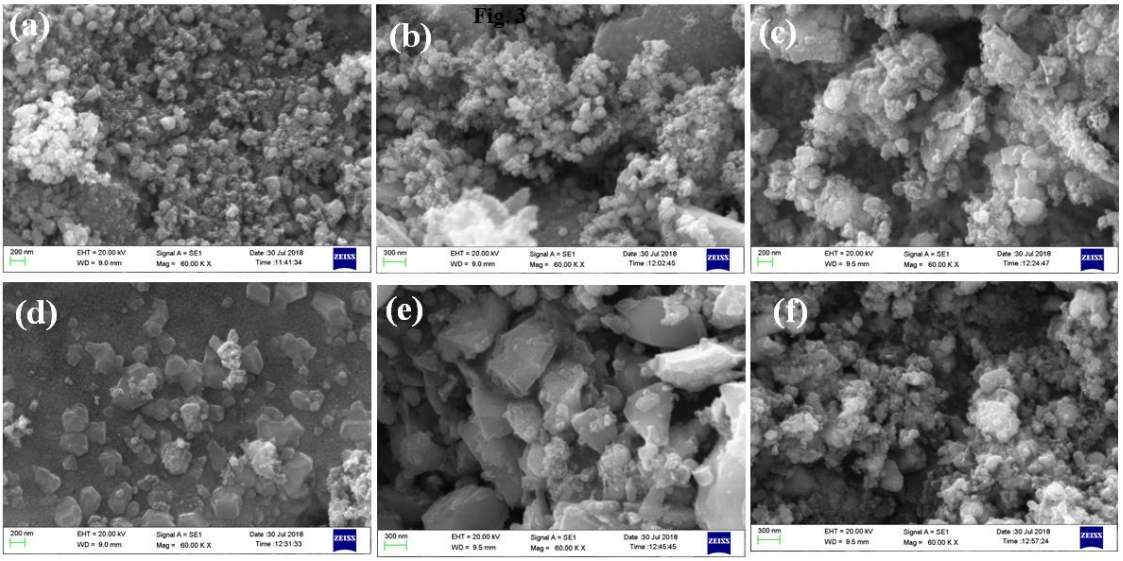

Figure 3.8 SEM images of (a) NFO-600, (b) NFO-700, (c) NFO-800, (d) NFO-900, (e) CFO-800, and (f) CNFO-800.

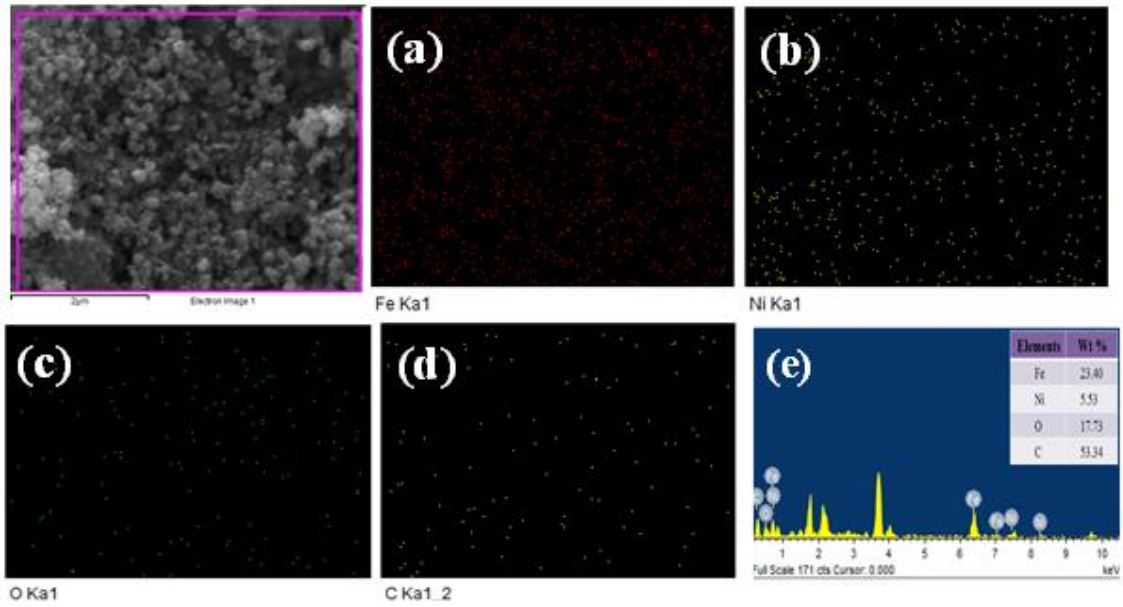

Figure 3.9 EDS Elemental mapping analysis of the underlined area in NFO-600.

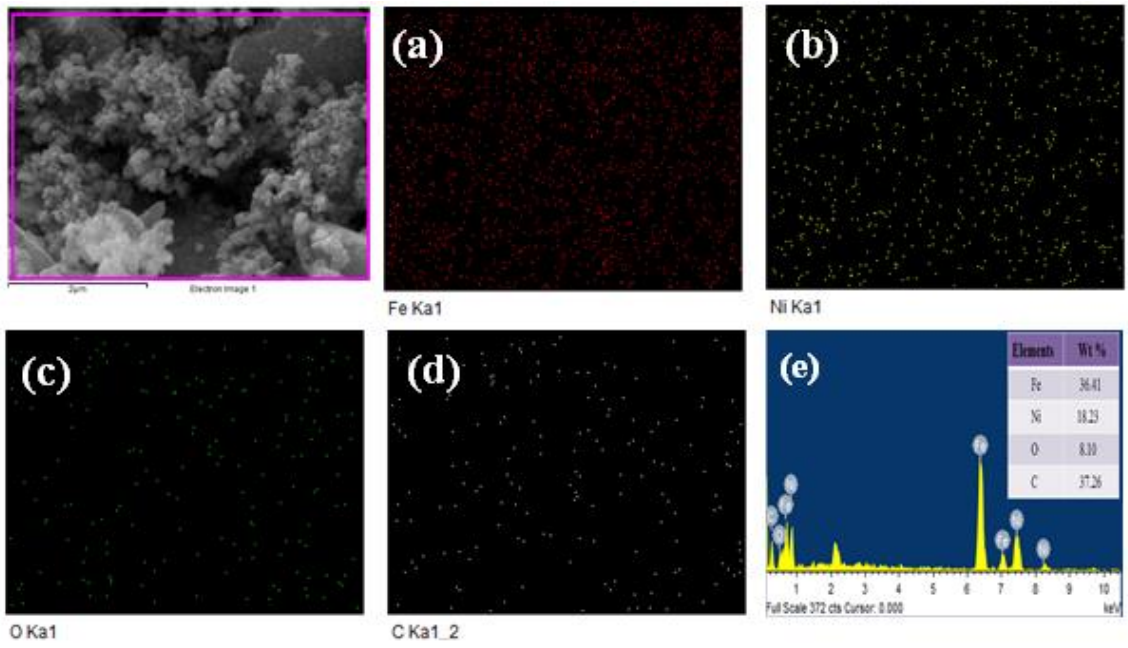

Figure 3.10 EDS Elemental mapping analysis of the underlined area in NFO-700.

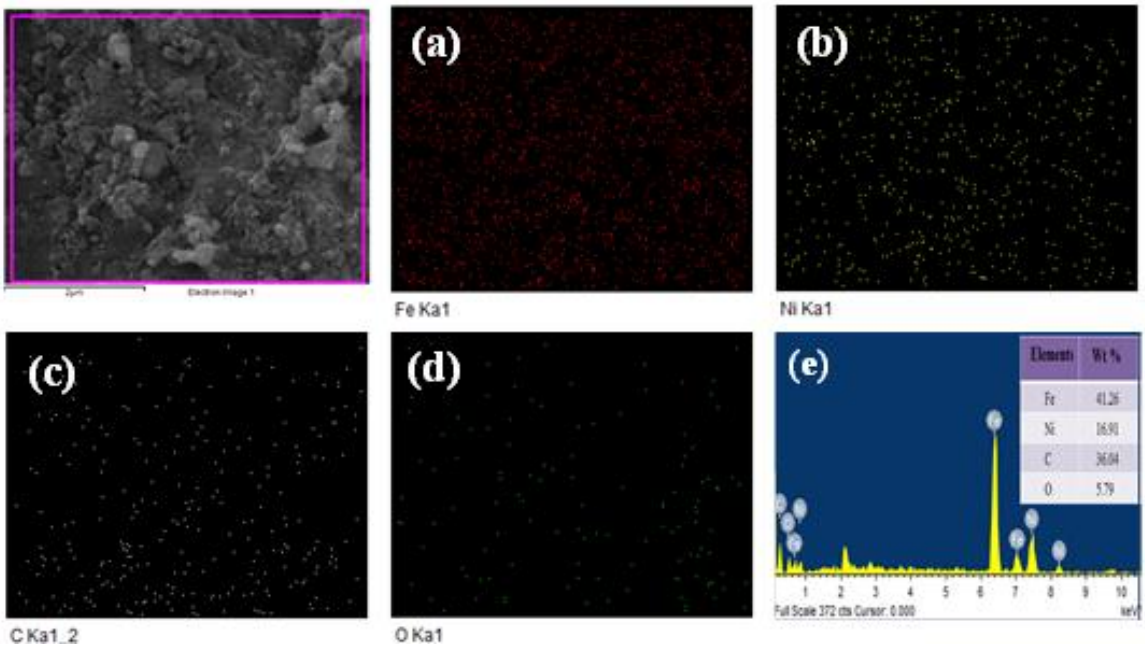

Figure 3.11 EDS Elemental mapping analysis of the underlined area in NFO-800.

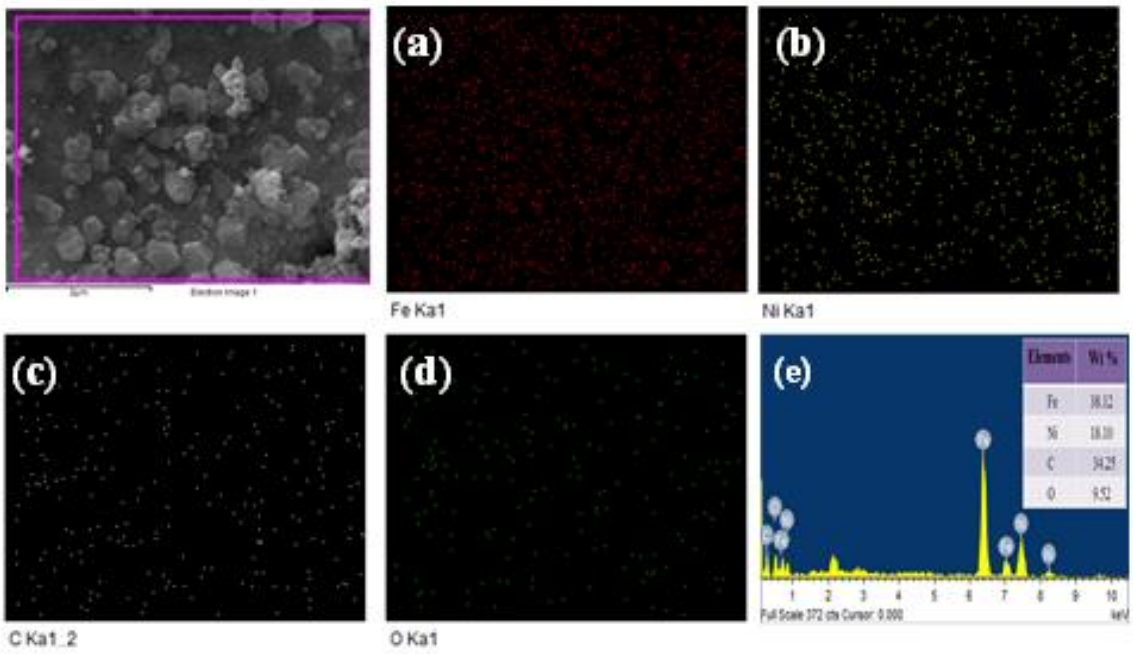

Figure 3.12 EDS Elemental mapping analysis of the underlined area in NFO-900.

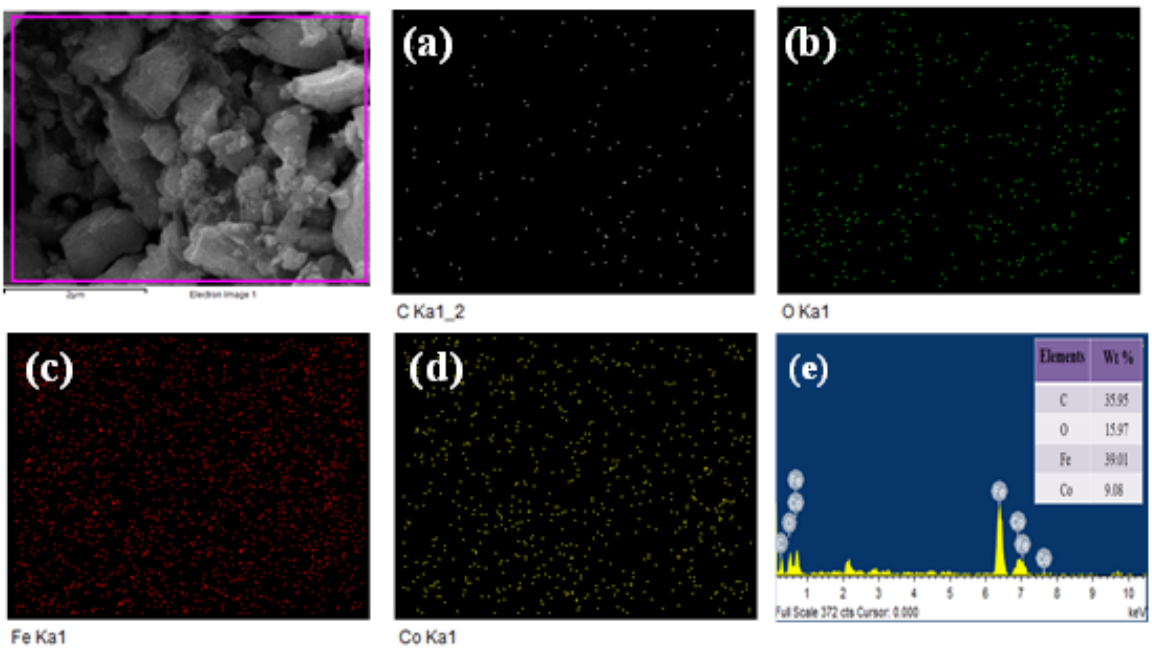

Figure 3.13 EDS Elemental mapping analysis of the underlined area in CFO-800.

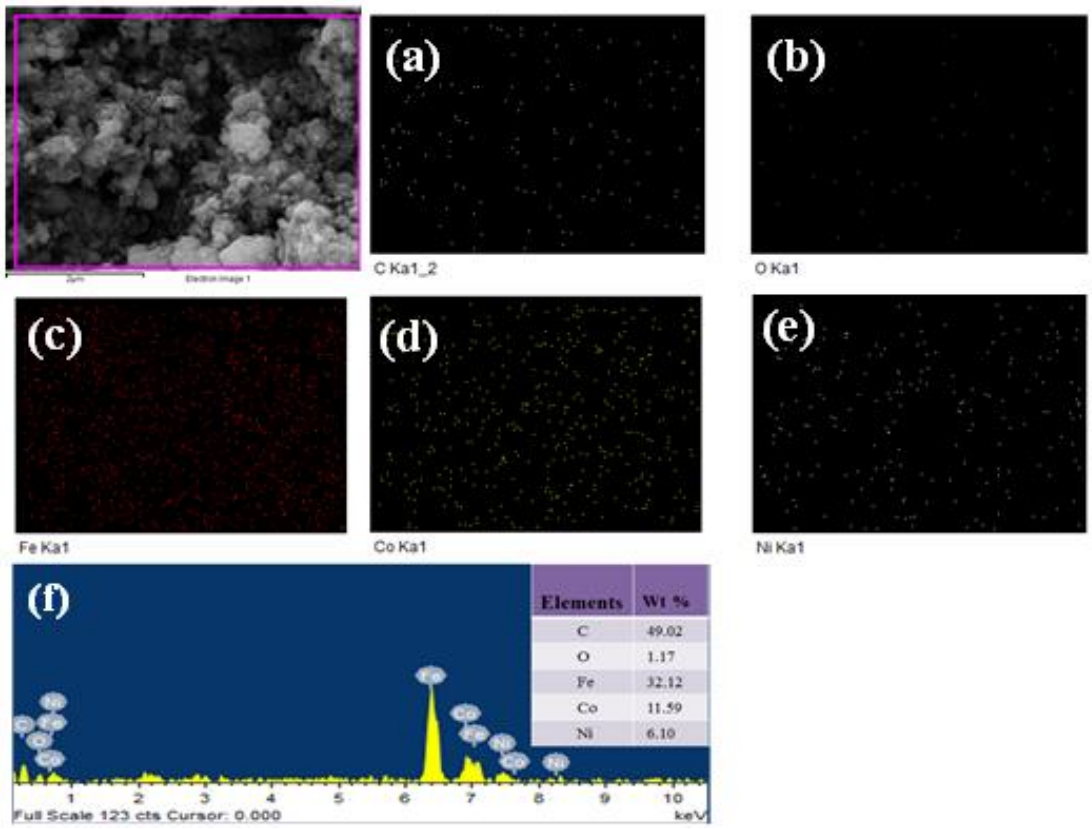

Figure 3.14 EDS Elemental mapping analysis of the underlined area in CNFO-800.

3.2.5 Oxygen Evolution Study

The catalytic performance of all the prepared catalysts was studied by linear sweep voltammetry and electrochemical impedance spectroscopy. Figure 3.15(a) shows the LSV of nickel ferrite synthesized at different temperatures (NFO-600, NFO-700, NFO-800 and NFO-900 °C). As depicted in Figure 3.15(a) with increasing temperature (from 600 to 800 °C) catalytic current increases and above 800 °C, loss in catalytic activity was observed. This could be due to collapsing the structural morphology, which can be clearly seen from SEM images [Figure 3.8(d)] *(vide supra*). Further, we have compared the OER performance of NFO-800 with CFO-800, CNFO-800, and RuO_2. LSV of these catalysts have been shown in [Figure 3.15(b)], and the respective onset potential was found to be 1.52, 1.59, 1.53 and 1.46V. The overpotential (η) for NFO-800 was found to be 280 mV which is very close to the overpotential of state-of-the-art catalysts RuO_2 (240 mV). Overall it was found that NFO-800 and CNFO-800 show almost similar OER activity and CFO-800 shows the least OER activity. The variation in catalytic performance could be due to different oxygen vacancies in the respective catalysts. From XPS measurement oxygen atomic weight percentage in CFO-800, NFO-800 and CNFO-800 was found to be 39.63, 13.05 and 15.87 respectively. The oxygen vacancy can be examined through the percentage area of the chemisorbed oxygen peak in the O 1s XPS spectrum of NFO-800, CFO-800 and CNFO-800. The percentage area of the chemisorbed peak of O 1s is found to be 49%, 32% and 47% for NFO-800, CFO-800 and CNFO-800, respectively. As can be seen, NFO-800 and CNFO-800 have almost similar oxygen vacancies which are higher as compared to CFO-800. Liu et al. have reported the role of oxygen vacancy on OER performance and found that more the oxygen vacancy more is the OER performance [141]. Due to oxygen vacancy excess electrons are generated and help in binding the adsorbate to the surface of the catalysts via surface-to-adsorbate [126, 152].

It was found that oxygen-deficient materials have more influence on OER overpotential as compared to their stoichiometric materials. In our case also, NFO-800 and CNFO-800 have more oxygen vacancy as well as OER performance. Present finding trends were further justified via BET surface area analysis. From BET measurements, we found that although CFO-800 have a higher surface area and pore size, its OER performance was lower as compared to NFO-800 and CNFO-800. Almost identical surface area and pore size were found in the case of NFO-800 and CNFO-800 (*vide supra*) which were lesser as compared to CFO-800. From XPS and BET analysis, we conclude that oxygen vacancy plays playing dominating role in OER as compared to pore size and surface area. For the comparison of the performance of the synthesized composites, first of all, we have calculated the Tafel slopes of NFOs prepared at various temperatures [Figure 3.15(a')] and minimum Tafel slope (93 $mVdec^{-1}$) and overpotential (~300 mV) was observed for NFO-800 and beyond this temperature rise in overpotential, and Tafel slope was observed which could be due to collapsing of the structural morphology (*vide supra*) which can be clearly seen in SEM [Figure 3.8(d)]. Further, we have also estimated the Tafel slopes of cobalt ferrite CFO-800 and cobalt substituted nickel ferrite CNFO-800 [Figure 3.15(b')]. It was found that NFO-800 and CNFO-800 show similar OER performance in terms of Tafel slope and overpotential. Thus we can say that no significant improvement in the OER performance of NFO-800 was obtained after substituting with cobalt. The performance of prepared catalysts was found to be superior or comparable to previous $NiFe_2O_4$ nanoflower and nanoparticles prepared by electrospinning and sol-gel method, respectively [153].

Further, an EIS study was applied to examine both the charge transfer kinetics and the adsorption of intermediates at the electrode interface. Nyquist plots of NFOs (NFO-600, NFO-700, NFO-800 and NFO-900) and with other cobalt doped spinels (CFO-800 and

CNFO-800) have been shown in [Figure 3.16(a) and (b)], respectively, which were measured at overpotential (η) of 346 mV. In the case of all the electrodes, two semicircles were observed in high as well as in low-frequency regions which are mainly associated with metal oxide and OER assets of the catalysts. Semicircle observed at low-frequency region is mainly due to adsorption/desorption of (H^+/OH^-) reactive intermediates by relaxation and diffusion of charge-associated surface intermediates whereas at high frequency is the response of charge transfer resistance (Rct) [124, 154].

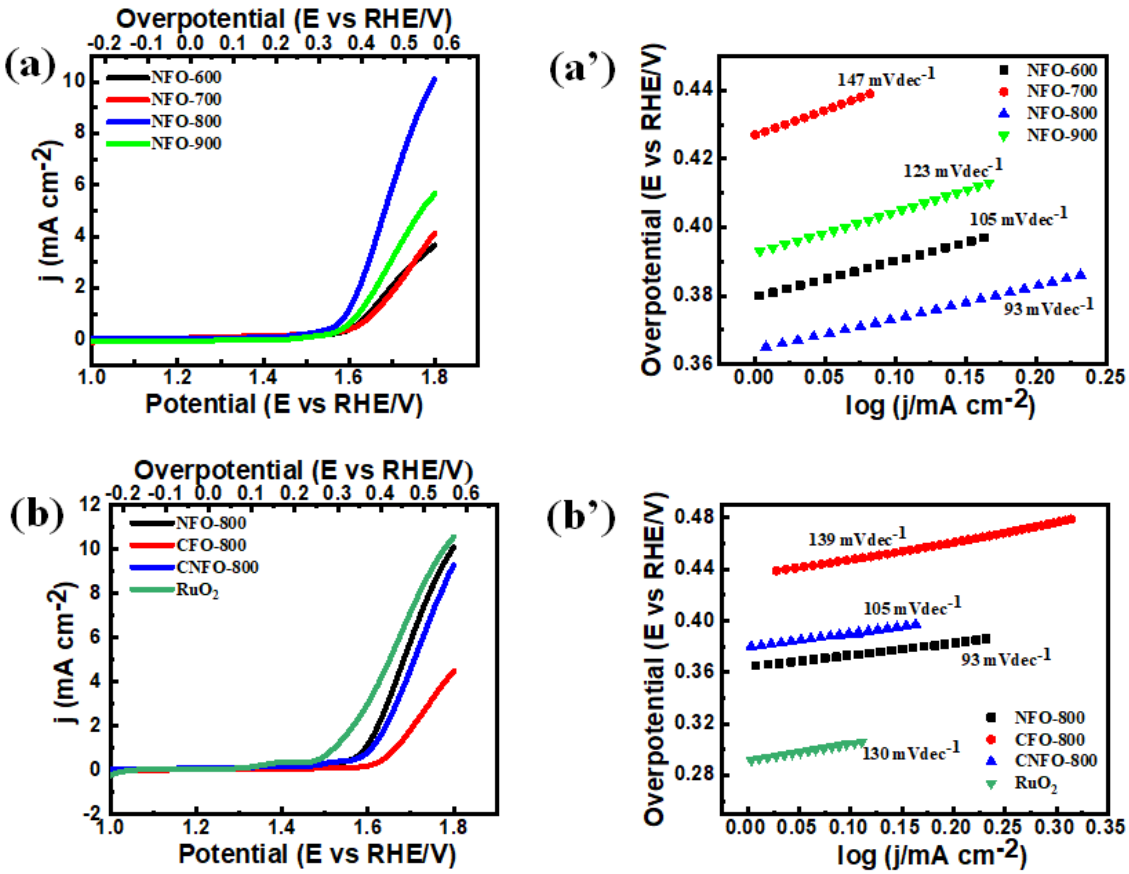

Figure 3.15 (a) Liner sweep voltammograms of NFO-600, NFO-700, NFO-800 and NFO-900 and (a') corresponding Tafel plots. (b) Liner sweep voltammograms of NFO-800, CFO-800 and CNFO-800 and (b') corresponding Tafel plots. Liner sweep voltammograms were recorded at a scan rate of 5 mVs^{-1} in 0.1 M KOH.

Although, for the calculation of impedance parameters various circuit models were tried, the best fit was found with R(QR)(QR)(CR) circuit only. It was found that NFOs and cobalt-doped NFOs both show capacitive as well as OER behaviour. As we know that

impedance is mainly controlled by the resistance and capacitance of the system, which gives total charge transfer resistance. The parameters estimated from the best-fitted circuit which explains the behaviour of the electrode have been tabulated in Table 3.2. The diagrams of the best-fit circuit have been shown in the insert of Figure. 6a, which contains various elements such as solution resistance (R_{so}), charge transfer resistance and constant phase element (QPE). Distribution of the resistance can be analysed with QPE which contains Y and α, where Y denotes the modulus of QPE and α denotes the distribution quality. For capacitive surfaces, the value of α varies from 0.6 to 1. Capacitance and resistance in medium frequency regions are denoted as C and R_{cap}. R_{so} is associated with solution-induced resistance at the interface of the electrode/electrolyte; R_{ct} and CPE are related to OER through adsorption/desorption of H^+/ OH^-, by diffusion, charge transfer resistance at the electrode or catalyst surface [4, 36-38]. From [Figure 3.16(a)], it is very clear that R_{ct} decreases from NFO-600 to NFO-800 from the low-frequency region and medium-frequency region, and further beyond 800 °C, it again increases. This EIS result is in well agreement with OER LSVs [Figure 3.15(a)] for this also the probable reason could be collapsing of the structure above 800 °C. Figure 3.16(b) shows EIS spectra NFO-800, CFO-800 and CNFO-800, among which NFO-800 shows the highest conductivity (least R_{ct}) and CFO-800 the least conductivity (highest R_{ct}). It was observed that after the substitution of cobalt in nickel ferrite, conductivity decreases than the pure $NiFe_2O_4$, that's why the R_{ct} of NFO-800 is lesser than CNFO-800, and CNFO-800 show their better catalytic activity and faster electron transfer rate than compared to the CFO-800. These EIS findings are also supported by LSV studies [Figure 3.15(b)] of NFO-800, CFO-800 and CNFO-800 (*vide supra*).

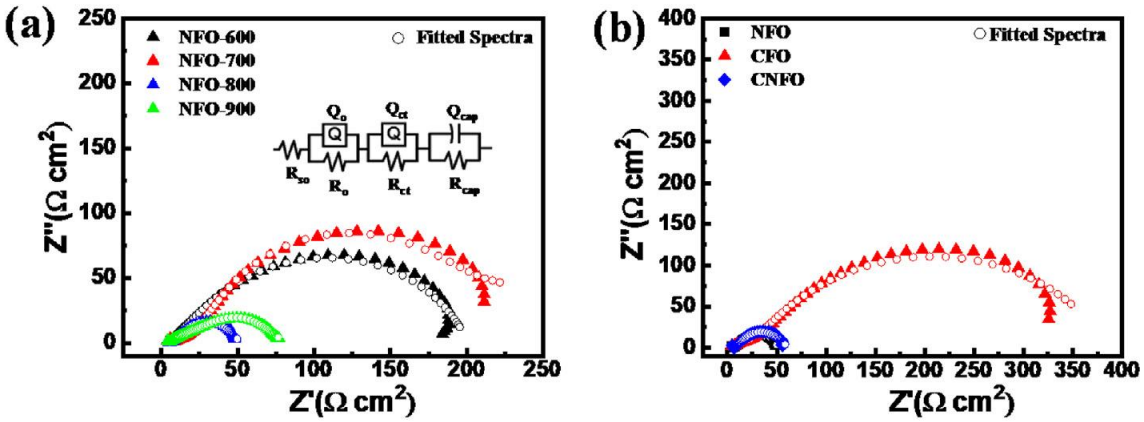

Figure 3.16 (a) Electrochemical impedance spectra of NFO-600, NFO-700, NFO-800 and NFO-900 and (b) electrochemical impedance spectra of NFO-800, CFO-800 (inset graph representative equivalent circuit) and NCFO-800.) Impedance was measured at an applied potential of 346 mV of η in 0.1 M KOH solution.

Table 3.2 Electrocatalytic impedance parameters of the catalysts.

Electrodes	R_{so} (Ωcm^2)	Q_O ($\Omega^{-1}cm^2S^{\alpha}$)		R_O (Ωcm^2)	Q_{ct} ($\Omega^{-1}cm^2S^{\alpha}$)		R_{ct} (Ωcm^2)	C (Fcm^2)	R_{cap} (Ωcm^2)	Z_{error} (%)
		Y_o	α_o		Y_{ct}	α_{ct}				
NFO-600	0.00094	6.94×10^{-7}	0.89	5.02	5.04×10^{-3}	0.55	131.7	6.25×10^{-3}	74	2.67
NFO-700	0.72	5.63×10^{-3}	0.45	15.9	6.91×10^{-3}	0.78	231.6	1.56×10^{-7}	6.36	2.35
NFO-800	0.0011	5.77×10^{-7}	0.89	5.48	2.45×10^{-2}	0.46	25.77	1.92×10^{-2}	22.02	2.16
NFO-900	0.018	1.51×10^{-7}	1	4.63	6.63×10^{-3}	0.45	59.05	1.66×10^{-2}	18.21	1.91
CFO-800	3.84	2.55×10^{-3}	0.44	35.27	3.72×10^{-3}	0.74	227.9	2.69×10^{-2}	98.26	2.99
CNFO-800	1.20	4.56×10^{-2}	0.35	7.57	1.12×10^{-2}	0.81	46.73	2.38×10^{-7}	4.7	2.13

3.2.6 Mechanism of OER

The OER is believed to occur through adsorption and discharge of OH^- at the active site of metal (S). The reaction proceeds via electrosorption of OH^- ions and a series of intermediates of S-OH, S-O, S-OOH, and S-OO via the bounded S-O followed by the formation of an O-O bond. Based on the literature and present study the mechanism can be proposed for oxygen evolution as given in [1.3.1.1(a)] [155-157, 23]. The higher catalytic performance of NFO-800 compared to CNFO-800 and CFO-800 could be due to the presence of more oxygen vacancies as measured through XPS. Maruthapandian et

al. [156] also used $NiFe_2O_4$ and cobalt-doped $NiFe_2O_4$ for OER studies and found that during OER, Ni in octahedral sites get oxidised from Ni^{2+} to Ni^{3+}/ Ni^{4+} and lower valence state of Ni gets stabilized by Fe and the higher oxidation state of Ni^{3+}/Ni^{4+} becomes electronically more conducting as compared to other doped metal [158-160]. In our case, we have doped NFO with Co, and the observed catalytic performance was lower or comparable to NFO, which is clearly visible in LSV also [Figure 3.15(b)].

Durability and operational stability are other important factors for any catalyst before getting commercialized. To access the durability and stability study of we performed the continuous CVs of best catalysts NFO-800 from 0.98 - 1.8V vs. RHE at a scan rate of 100 mVs^{-1} for 500 continuous cycles. It was found that no significant change in onset potential and current density was observed (Figure 3.17). This reveals the superior operational stability of NFO-800 towards OER application.

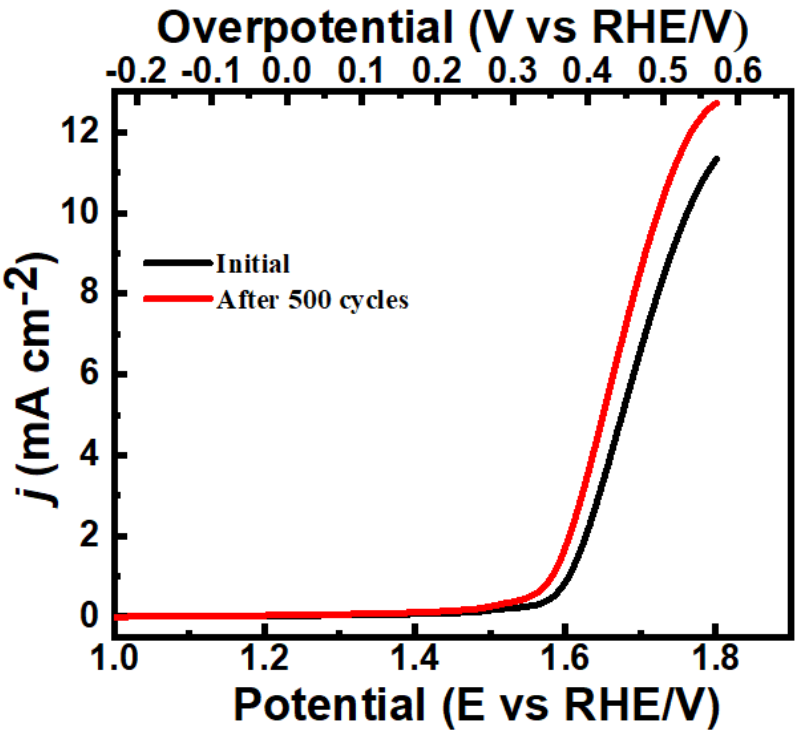

Figure 3.17 Linear sweep voltammograms of NFO-800 before and after 500 continuous CV cycles.

3.3 Conclusions

In conclusion, we have prepared spinel material by facile sol-gel technique and used the same for oxygen evolution application in an alkaline medium at room temperature. It was found that the OER performance of the prepared material was comparable to previously reported spinel-based material. Among all the materials, better performance was found for nickel-based spinel material, this could be due to increased oxygen vacancy, which is responsible for improved catalytic performance. Increased oxygen vacancy was confirmed by XPS and BET measurements.